Understanding and Exploiting the Optical Properties of Laser-Induced Quasi-Random Plasmonic Metasurfaces

Van Doan Le, Balint Eles, Nicolas Dalloz, Manuel A Flores Figueroa, Francis Vocanson, Christophe Hubert, Nathalie Destouches

ACS APPLIED OPTICAL MATERIALS

pubs.acs.org/acsaom Article

Understanding and Exploiting the Optical Properties of Laser-Induced Quasi-Random Plasmonic Metasurfaces

Van Doan Le, Balint Eles, Nicolas Dalloz, Manuel A. Flores Figueroa, Francis Vocanson, Christophe Hubert, and Nathalie Destouches*

Cite This: *ACS Appl. Opt. Mater.* 2024, 2, 373−385 Read Online

ACCESS | Metrics & More | Article Recommendations | Supporting Information

ABSTRACT: Laser-induced structural colors have the potential for industrial implementation thanks to their versatility, efficiency, cost-effectiveness, and simplicity. However, the quasi-random nature of the nanoparticle (NP) distributions produced by lasers has made the understanding of their optical properties tricky and the confidence in their reproducibility limited. In this article, we demonstrate the potential of nanosecond lasers to control the diffraction, dichroism, and colors of random plasmonic metasurfaces while explaining the origin of their optical properties through electromagnetic simulations. The optical properties are first linked to the geometrical parameters of self-organized gratings that are induced by laser either on the surface by topographic modulation or below the surface by the growth of organized NPs. These two kinds of gratings are perpendicular to each other and exhibit different periods. The article unravels the main mechanisms that shape the spectral properties of these laser-induced NP gratings. Electromagnetic simulations evidence the role of hybrid resonances resulting from the far-field coupling of metallic NPs despite their size dispersion and relative disorder. They also demonstrate the impact of near-field coupling that leads to the hybridization of plasmonic modes of some particle pairs closely packed along the grating lines in these laser-induced structures. The article shows how the two kinds of self-organized gratings influence the diffraction and dichroism. Imperfections of laser-induced metasurfaces bring singular properties that do not exist in perfectly regular samples. They are used here to print faithful color images in different modes of observation and to use diffraction or dichroism as a security feature.

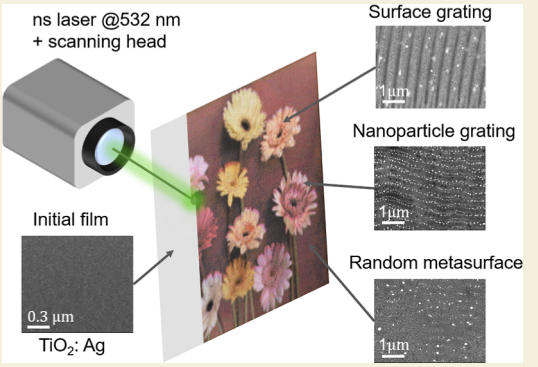

KEYWORDS: *laser processing, structural colors, self-organization, diffraction, dichroism, plasmonic nanoparticles*

INTRODUCTION

Structural color printing has emerged as an eco-friendly technique for generating vivid colors and interesting visual effects stable over time.[1−3] While traditional inks are based on dye absorption, structural color marking technologies create colors originating from various optical phenomena, including scattering,[4,5] absorption,[6,7] diffraction,[8] interference,[9] or coupling between resonance modes.[10,11] This gives the technologies huge advantages and extra freedom to design optical devices and develop real-life applications spanning from data storage,[12] information security,[13,14] color filters,[15] sensors,[16] to display technologies.[17]

Various approaches have been proposed to produce metamaterials with structural colors, such as electron beam lithography,[18,19] focused ion beam,[6] or chemical methods.[20] Among them, laser-based technologies emerge as foremost industrial processes owing to the fact that they are versatile, rapid, cost-effective, and scalable.[21,22] Laser can trigger several mechanisms that modify the physical properties of metamaterials and so their colors. Metallic particles can thus be resized, reshaped, and organized. The spectral shape of their localized surface plasmon resonances (LSPRs) can be tuned by changing their geometrical parameters.[23−28] When the laser triggers their self-organization, diffraction gratings whose period and orientation depend on the laser wavelength and polarization can emerge and be used to diffract visible light[29,30] or induce dichroism.[31,32] Dichroism refers to the color difference observed when samples are exposed to transverse electric polarization or transverse magnetic polarization of light. These diffractive and dichroic properties have recently been used to implement laser-induced image multiplexing for white light observation, where three images were encoded and printed on a single metasurface.[33,34] The dichroic colors that were used for some multiplexed images were shown to result from the coupling between the LSPR of individual metallic

Received: November 2, 2023
Revised: February 15, 2024
Accepted: February 22, 2024
Published: March 6, 2024

https://doi.org/10.1021/acsaom.3c00395
ACS Appl. Opt. Mater. 2024, 2, 373−385

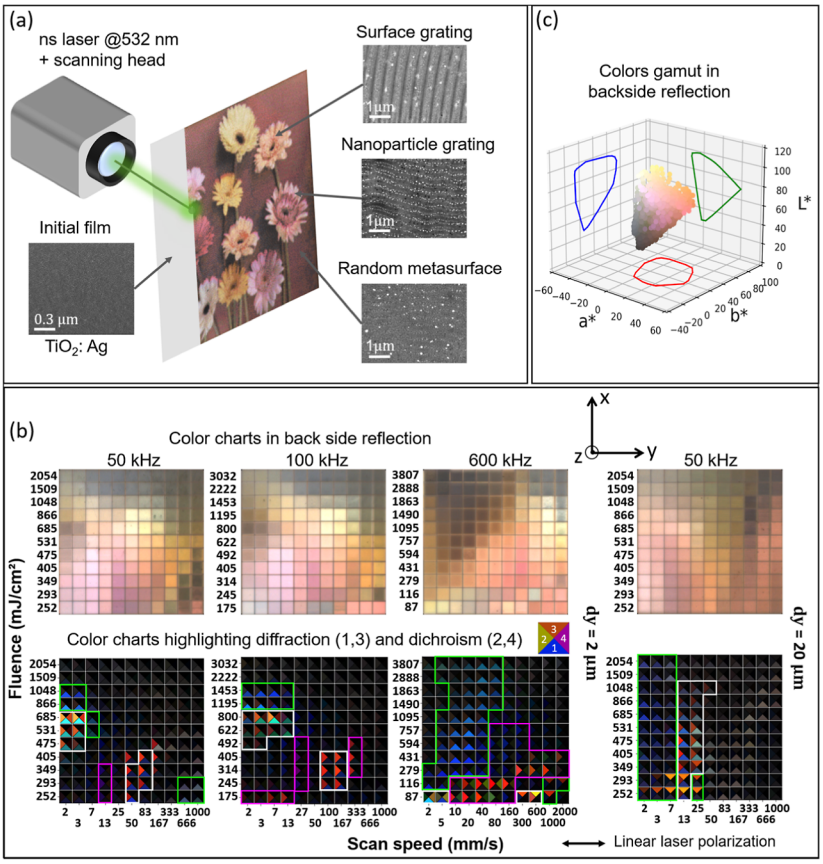

Figure 1. Optical properties of laser-induced metasurfaces. (a) Principle of the laser marking process. A few SEM images illustrate different kinds of laser-induced metasurfaces that exhibit different colors. (b) Charts illustrating some optical properties of metasurfaces generated by varying four laser processing parameters: the laser fluence and repetition rate, the scan speed of the laser beam, and the distance dy between consecutive laser lines. The laser polarization is fixed and parallel to the double arrow. The top charts show the colors observed in backside reflection. All measurements were carried out under white light illumination. The bottom charts show four data points per square. Triangles #1 and #3 show the color observed in two diffraction configurations where the plane of incidence is either parallel to the *xz* plane (triangle #1) or parallel (triangle #3) to the plane. Triangles #2 and #4 illustrate the dichroism in reflection and transmission, respectively, where the displayed color corresponds to the color difference (ΔR, ΔG, and ΔB) between the colors measured with a TE or TM linearly polarized incident white light. The setup used for measuring the colors is described in Figure S3. (c) Gamut in the CIE L*a*b* color space of colors measured in the backside reflection mode (CIE RGB color space and details are given in Figure S4). The convex hull of the gamut is projected on the three planes for more clarity.

particles and delocalized photonic modes excited through the self-organized nanoparticle (NP) grating.[34] In all these studies, the laser simultaneously modifies several parameters of metallic NPs, including their size, density, and organization, and does control the statistical distribution of these parameters over large ensembles of NPs rather than their specific values for each single particle. The laser can also change different parameters of the film that supports or contains the NPs, such as its crystal phase, density, thickness, or surface topography. Fabry−Pérot interferences can then contribute to the final optical properties of the system.[35,36] The variety of optical mechanisms involved in random plasmonic metasurfaces makes them powerful to create particular color properties, such as the ones that recently enabled three-image multiplexing. The simplicity and flexibility of laser processing make it appealing for the development of large-scale applications. Moreover, the quasi-random nature of the NP assemblies poses an interesting challenge in investigating how the different mechanisms shape the color properties of these materials.

In this paper, we unravel the mechanisms that control the optical properties of quasi-random plasmonic metasurfaces produced by laser processing. We especially pay attention to nanosecond (ns) laser-processed Ag NPs/TiO_2 metasurfaces that exhibit diffractive and dichroic properties to explain why these two phenomena can be observed simultaneously or independently. Optical characterizations highlight the laser parameter ranges where the different optical behaviors occur and allow rapid identification of the main kinds of metasurfaces that can be produced by laser processing. Their morphological properties are measured by electron microscopy and atomic force microscopy (AFM). Two main features, a periodic arrangement of metallic NPs and a periodic modulation of the surface topography, characterize the diffractive or dichroic metasurfaces. The article explains the relative importance of the different self-organized periodic structures in relation to the optical properties of metasurfaces. Electromagnetic simulations of as-fabricated samples unveil the role of coherent far-field coupling by the NP grating and of near-field coupling on the diffractive and dichroic properties. They allow us to explore separately the influence of different parameters by considering both the as-fabricated structures and close perfectly periodic structures. The paper finally demonstrates that the technology can be used to mark faithful color images in different observation modes. The colors observed in other modes can then be used for security purpose.

https://doi.org/10.1021/acsaom.3c00395
ACS Appl. Opt. Mater. 2024, 2, 373−385

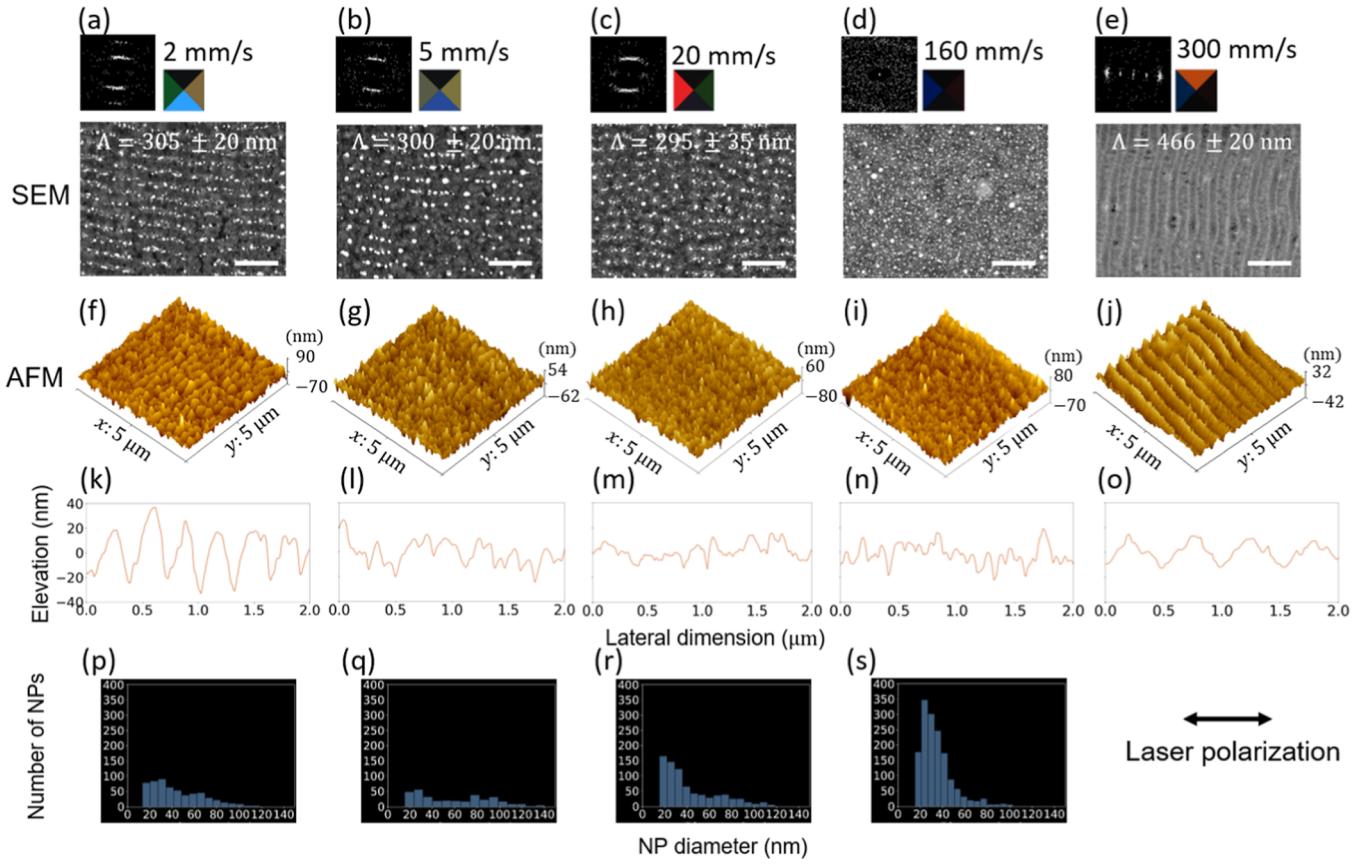

Figure 2. Evolution of the physical and optical properties of laser-induced metasurfaces when varying the scan speed (from 2 to 300 mm/s) at low fluence (87 mJ/cm^2), high repetition rate (600 kHz), and large overlapping between laser lines (dy = 2 μm). For each scan speed, the sample is characterized by a four-color chart (as described in Figure 1), a representative SEM image with the value of the grating period and its Fourier transform on the top corner left (a–e); an AFM 3D view of the surface topography (f–j) and the corresponding surface profile (k–o), measured along the *x*-axis for the 4 left images and along the *y*-axis for the sample at 300 mm/s; and a histogram of the NP sizes as observed by SEM (p–s). The double arrow indicates laser polarization for the SEM images. The scale bar is 1 μm in all the SEM images.

RESULTS AND DISCUSSION

Overview of the Optical and Structural Properties of Laser-Induced Random Plasmonic Metasurfaces

Mesoporous titania thin films loaded with silver and deposited on a glass substrate are processed with a slightly focused nanosecond laser (532 nm) scanning the surface. During the laser-induced processing, the films undergo several physical and chemical processes, including coalescence, Ostwald ripening, and reduction. These processes enable the reshaping and growth of metallic particles,[31,37,38] resulting in the creation of plasmonic metasurfaces. In addition, some films exhibit self-organizations of NPs or surface grating owing to the optical interference of the excited surface or guided modes with an incident wave as described in Section S1 of Supporting Information. This also contributes to the formation of self-organized plasmonic metasurfaces, as depicted in Figure 1a. Their properties are controlled at the scale of a pixel size (see Methods and Figures S1 and S2 for details about the initial material and laser processing) by varying four parameters. In Figure 1b,c, we present a sampling of colors exhibited by the metasurfaces in specular reflection when observed from the backside. The corresponding color measurements can be found in Figures S3 and S4 in the Supporting Information. A detailed discussion on the printing of faithful color images in various modes of observation will be provided at the end of the article (see section Printed Plasmonic Color Images).

Figure 1b highlights different diffractive and dichroic behaviors of metasurfaces. By simply tuning laser parameters, we can obtain samples that exhibit both diffraction and dichroism (squares inside white light) or dichroic and not diffractive (pink outline), and still a large part is diffractive without exhibiting any significant dichroism (green outline). The diffractive behaviors (triangles #1 and #3) highlight the presence of two main kinds of diffraction gratings that result from laser-induced self-organization processes.[31,32] The origin of the two perpendicular self-organized periodic patterns is discussed in the Supporting Information (Section S1). This decision aims to avoid overloading this review, which primarily focuses on investigating the optical properties of these laser-induced metasurfaces. The first type of self-organized grating, which appears when triangle #1 is lit in blue (Figure 1b, bottom color charts), corresponds to gratings parallel to the *y*-axis with a period in the range 290–380 nm. When the blue color shifts toward green in triangle #1, the grating period increases, as can be deduced from the grating equation and the fixed parameters of the measurement setup (Figure S1). Interestingly, this grating type can take various forms. It corresponds to periodic modulation of the surface topography with disordered NPs in Figure S5a. It may correspond to self-organized particles mainly located in the film, with additional surface corrugation (Figure S5b) or without surface corrugation (Figure S5c). Figure S7 shows self-organized

https://doi.org/10.1021/acsaom.3c00395
ACS Appl. Opt. Mater. 2024, 2, 373–385

particles that emerge on the top surface. The next section will investigate the influence of the particle properties on the observed diffraction properties. The second type, which appears when triangle #3 is lit in orange, corresponds to gratings parallel to the x-axis with a period in the range 460−500 nm. When the orange color shifts toward yellow in triangle #3, the grating period decreases, and the scanning electron microscopy (SEM) images are given in Figure S6. Some triangles (#1) appear whitish or brownish rather than blue; they correspond to metasurfaces that scatter light in a broad range of observation angles rather than diffracting it, indicating more disordered metasurfaces.

When the laser lines largely overlap (dy = 2 μm for a beam diameter of 13.5 μm), the metasurfaces are homogeneous over a pixel size, and the two kinds of gratings never occur simultaneously (Gratings #1 and #3 never lit on in the same square in Figure 1b for dy = 2 μm).

When the laser lines do not overlap (dy = 20 μm), gratings #1 and #3 can be observed simultaneously on the same pixel (Figure 1b, 13 mm/s at low fluence). In this case, grating #1 forms in the beam center, where the fluence is higher, while grating #3 forms on the beam edge, where the fluence is lower (Figure S7). The former gains spatial extent over the latter when the fluence increases.

Triangles #2 and #4, in Figure 1b, characterize the sample dichroism that is shown by a color corresponding to the (ΔR, ΔG, ΔB) difference between the colors measured with TE (where the polarization aligns with the y-axis) or TM (parallel to the x-axis) polarized white light. All these samples are composed of self-organized NPs grating, with some additionally featuring surface gratings (as shown in Figure S5b,c).

Before delving into the investigation of how NP gratings influence dichroism and diffraction, let us first conduct a more comprehensive analysis of the surface morphology and NP gratings of these samples. This will enable us to gain a deeper understanding of the impact of the structural parameters of quasi-random plasmonic metasurfaces on their optical properties.

Structural Parameters of Metasurfaces

To make this analysis comprehensive, we propose studying their evolution when varying only one laser parameter. We choose to display the evolution of the surface topography and metallic NPs with the scan speed for metasurfaces generated at low fluence (87 mJ/cm^2), high repetition rate (600 kHz), and strong overlapping between laser lines (dy = 2 μm), where the surface profiles vary strongly, leading to very different diffractive and dichroic properties of the induced metasurfaces, as a function of scan speed. As illustrated in Figure 2, at low speed, these metasurfaces exhibit diffraction with grating parallel to the laser polarization (#1) and dichroism (#2 and #4) (Figure 2a). Then, when speed increases, only dichroism is observed (Figure 2b,c) before disappearing (Figure 2d). At the highest speed, diffraction by a grating perpendicular to the laser polarization (#3) occurs (Figure 2f). The combination of SEM and AFM images gives insight about the main features that characterize the metasurfaces, namely, their surface topography and the distribution of metal NPs (Figure 2a−g). At 300 mm/s, the self-organized gratings perpendicular to the laser polarization (#3) are surface gratings whose period is slightly lower than that of the laser wavelength, in which Ag NPs are small enough not to be clearly observed by SEM. When decreasing the scan speed (160 mm/s), i.e., increasing the deposited energy per unit area, the surface topography homogenizes, the grating disappears, and Ag NPs grow within a correlated disorder (homogeneous distances between NPs). From 20 to 5 mm/s, NPs tend to organize along grating lines parallel to the laser polarization while growing up to reach sizes that exceed 100 nm. The reduced particle count observed at a scanning rate of 5 mm/s can be attributed to the presence of tiny particles or particles deeply embedded along the grating lines that could not be detected. At the lowest speed, Ag NP gratings are associated with a surface grating that follows the NP lines (same orientation, same period). The period of the NP gratings is a fraction of the laser wavelength, and the divider is expected to be the effective refractive index of the photonic mode that can propagate within the layer (as explained in Supporting Information Section S1).

These results highlight the strength of diffraction through the brightness of diffractive colors shown in triangles #1 and #3. The measurement conditions in diffraction are detailed in Section S2 of the Supporting Information. Color is observed in triangle #1 when a diffraction grating is formed parallel to the laser polarization and in triangle #3 when the diffraction grating aligns perpendicularly to the laser polarization. Then, the higher the diffraction efficiency, the higher the brightness of the colored triangle. A change in the grating period results in a change in the triangle hue. Based on these experimental results, it appears that the diffraction efficiency may be due to a surface grating or an NP grating embedded in the layer or to a combination of both. The NP grating contributes to diffraction through coherent far-field coupling, and its diffraction efficiency is weakened by heterogeneity in the NP arrangement and broad size distributions.[32] Conversely, in these experiments, dichroism appears to be primarily associated with self-organized NP gratings rather than surface gratings, as evident in Figure 2 with the metasurface at a scan speed of 20 mm/s. Strong dichroism is observed due to NP self-organization (Figure 2c), even in the absence of a surface grating, as confirmed by the associated AFM characterizations (Figure 2h,m). This dichroism is expected to originate primarily from two mechanisms: the near-field coupling between NPs aligned along the same line and the far-field coupling between the localized surface plasmon mode through the excitation of a delocalized photonic mode propagating perpendicular to the grating lines.[39] In the following sections, we will elucidate the underlying mechanisms in the optical responses of laser-induced quasi-random plasmonic metasurfaces. Our investigation will encompass both as-fabricated samples and regular samples (periodic structures with a single NP size). We will explore the influence of structural parameters of laser-induced NP gratings on the diffractive and dichroic properties of metasurfaces.

Origin of Dichroism

In order to unveil the optical mechanisms at the origin of dichroism in the laser-induced metasurfaces, we propose to simulate the electromagnetic far-field response of an as-fabricated sample that mimics a dichroic experimental sample as well as its closest regular sample (periodic and single NP size), which exhibits similar spectral features. Investigating the near-field of the regular sample will demonstrate the origin of collective resonances and serve as a guide to finding similar resonances in the as-fabricated sample. Some features that are specific to the realistic samples will finally appear to strongly contribute to the dichroism too.

https://doi.org/10.1021/acsaom.3c00395
ACS Appl. Opt. Mater. 2024, 2, 373−385

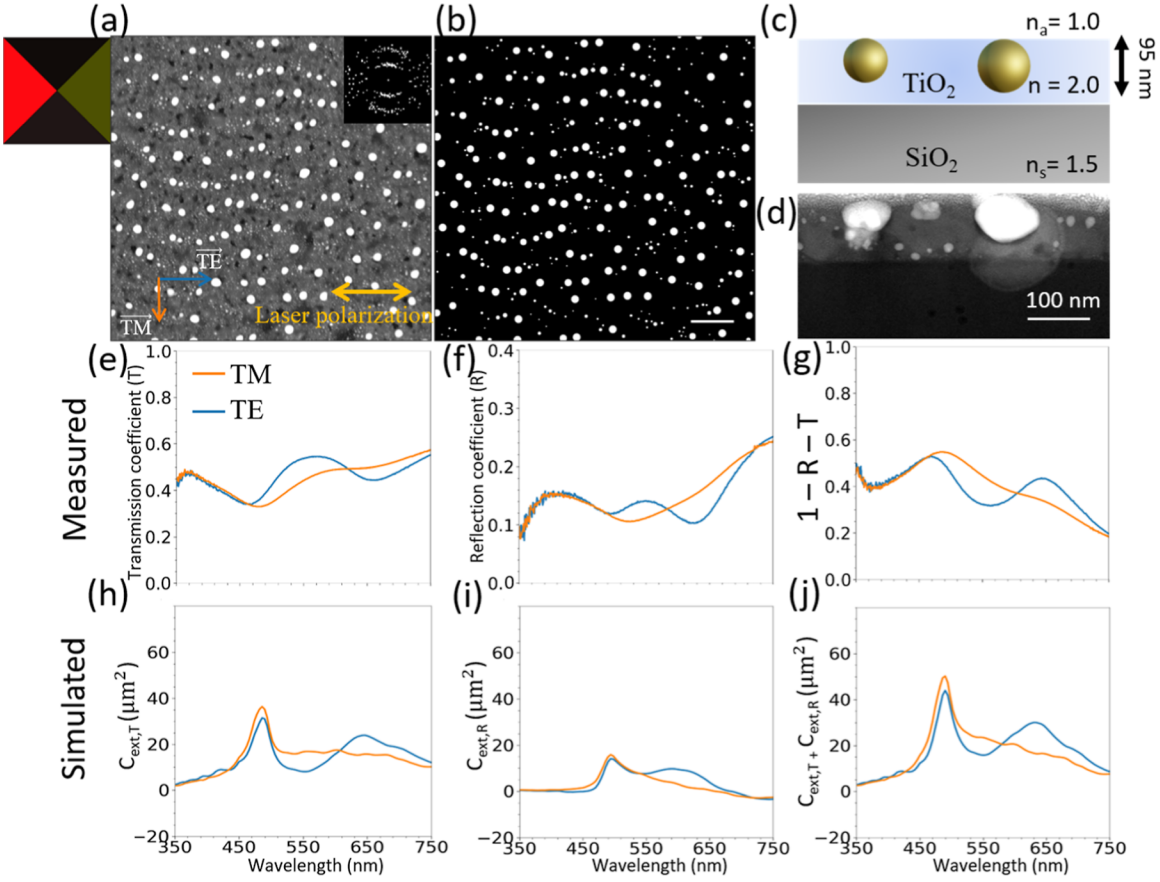

Figure 3. Experimental vs simulated results of the as-fabricated sample. (a) SEM image of the considered nanostructure induced by laser processing at 600 kHz, 116 mJ/cm^2, 80 mm/s^1, and dy = 2 μm, with the image Fourier transform in inset. (b) Plane view and (c) cross section of the simulated as-fabricated sample. (d) TEM cross section of the experimental sample. (e,f) Experimental data of transmission (T) and reflection coefficient (R), and (g) the corresponding loss spectrum (1 − T − R). (h−j) Simulation results of extinction cross section in transmission ($C_{ext,T}$), reflection ($C_{ext,R}$), and total extinction ($C_{ext,T}$ + $C_{ext,R}$), respectively. Scale bar in SEM (b) is 500 nm. The incident field illuminates from the bottom at an incidence angle of θ = 6° with a vertical incidence plane. The NP grating lines are parallel to the linear polarization of the laser used for processing the sample (horizontal double arrow in part a).

Figure 3a,d shows the SEM plane-view and TEM cross-sectional images of a dichroic sample (triangles #2 and #4 lit) obtained at 600 kHz, 116 mJ/cm^2, 80 mm/s, and dy = 2 μm. A tridimensional representation of this sample is elaborated by considering spherical NPs with the same diameter and in-plane distribution as those measured by SEM, and an in-depth location compatible with the simulation constraint imposes that NPs must be located within a single medium. In the simulation, all NPs are tangential to the top interface inside the 95 nm TiO_2 layer (Figure 3b,c). As the initial mesoporous TiO_2 layer (initial film thickness of ∼200 nm as described in Methods section) has been largely densified by laser processing and the initial amorphous TiO_2 has been crystallized into its anatase phase, a 95 nm anatase TiO_2 layer with Raman characterization is created, as shown in Figure S8. To simplify the analysis, we approximate the refractive index of the surrounding film, which encompasses anatase TiO_2 and small silver particles (as shown in Figure 3d), as 2, while the glass substrate is assumed to have a refractive index of 1.5. Further details about the refractive index of Ag NPs and numerical parameters used for simulations are given in the Methods section. To reduce numerical errors due to the limited sample size (and number of NPs), the as-fabricated sample is extended by duplicating four times the same structure.

The simulated extinction cross-section spectra in transmission and reflection (Figure 3h,i) of the as-fabricated sample, which account for losses in the two specular directions, can be compared qualitatively with the transmission (T) and reflection (R) coefficients (actually with 1-T and 1-R) measured on the experimental sample (Figure 3e,f), for two linear polarizations are parallel (TE) or perpendicular (TM) to the NP grating lines (themselves parallel to the laser polarization used during laser processing). The total experimental losses (Figure 3g) can also be compared to the total simulated losses (Figure 3j). In both cases, the losses exhibit a single broad peak for TM polarization and two peaks for TE polarization.

In Figure 4, we compare the far-field spectra and near-field intensity distribution of the as-fabricated sample with those of a regular sample in which all NPs are 71 nm in diameter and periodically spaced with a 300 nm period along the x direction and a 180 nm period along the y direction [Figure 4a(i)]. This regular sample exhibits narrower resonances and homogeneous near-field maps that make interpretation easier [Figure 4a(ii)]. If the period along the x direction is similar to the average period that can be measured between lines of the as-fabricated sample, the periodicity along the y direction is a stronger simplification since it does not exist in the realistic sample.

https://doi.org/10.1021/acsaom.3c00395
ACS Appl. Opt. Mater. 2024, 2, 373−385

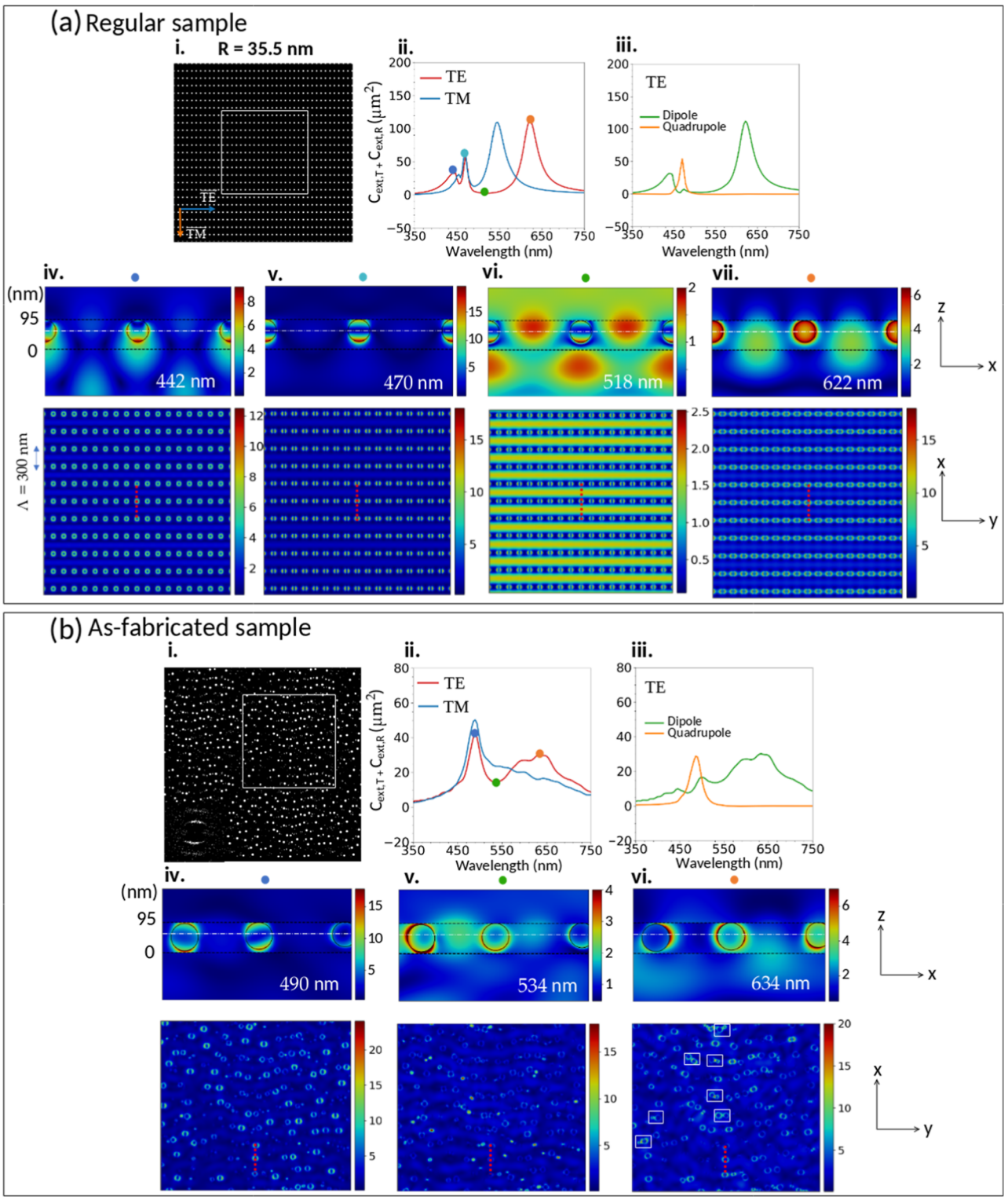

Figure 4. Near-field maps in *xz* and *xy* planes of the regular and as-fabricated samples in TE polarization. Plane view of the (a(i)) regular and (b(i)) as-fabricated simulated samples. Image (b(i)) contains the Fourier transform of the plane view in insert. Spectral variations of the total extinction for the (a) regular and (b) as-fabricated samples for TE and TM polarizations. Multipole decomposition of the total extinction for the (a(iii)) regular and (b(iii)) as-fabricated samples for TE polarization. (a(iv)−(vii),b(iv)−(vi)) Cross section and plane view of the near-field intensity for TE polarization at selected wavelengths that are identified by disks with different colors in (a(ii),b(ii)), respectively. The plane-view near-field maps are calculated along the white dashed−dotted lines drawn in the cross-section maps and correspond to the areas limited by a white rectangle in (a(i),b(i)), respectively. The cross-section near-field maps are calculated along the red dotted lines drawn in plane-view maps. The black dashed lines show the layer interfaces. Illumination from the bottom side was performed with an incidence angle $\theta = 0°$.

However, the regular sample has strong enough similarities to provide a useful comparison with the as-fabricated sample.

For TM polarization, the regular sample exhibits a main peak at 545 nm for the dipolar mode [Figures 4a(ii) and S10].

https://doi.org/10.1021/acsaom.3c00395
ACS Appl. Opt. Mater. 2024, 2, 373−385

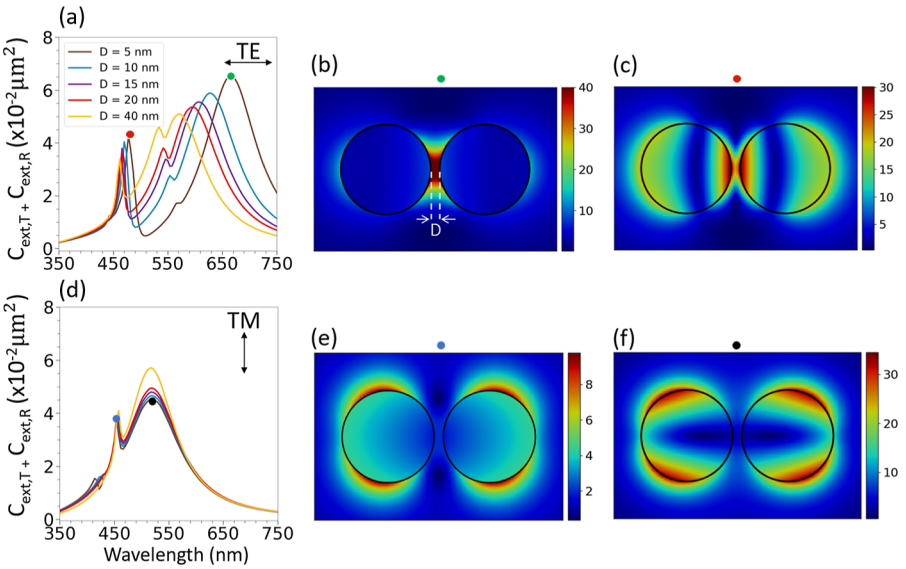

Figure 5. Near-field coupling. (a,d) Total extinction cross section of a dimer in the layer system with varying interparticle distances for TE (along the dimer axis) and TM (perpendicular to the dimer axis) polarizations, respectively. Field enhancement in plane view for dipolar (b,e) and quadrupolar (c,f) resonances for both polarizations. The particle size is 50 nm in diameter.

For TE polarization, the main peak of the dipolar mode red-shifts at 622 nm and is accompanied by a second peak at 442 nm [Figure 4a(iii)]. A quadrupolar mode is added at 470 nm. The long-wavelength peak results from the far-field coupling of the localized surface plasmons of the individual NPs. For an appropriate period of the NP grating, the field scattered by the NPs arrives in a phase with the LSPR induced by the incident field on adjacent particles, thereby reinforcing the resonance [Figures 4a(vii) and S11g]. This effect is known as a hybrid plasmonic photonic resonance, which leads to an extinction enhancement at 622 nm and a short-wavelength peak with lower amplitude. In this hybrid coupling, the photonic mode is associated with the guided mode resonance supported by the TiO_2 layer. Similar behavior of the hybrid resonances is also reported in some articles.[41,42] In our layered system, the field enhancement at 442 nm is maximum on the bottom side of NPs and along the TE incident field [Figure 4a(iv)]. For TE polarization (along the *y*-axis), we can also highlight at ∼518 nm the guided mode excited through diffraction by the NP periodic array that propagates along the *x* direction π out-of-phase with the incident field on metallic NPs.[40] The destructive interference of the propagating mode with the incident field on the NPs considerably reduces the NP absorption and leads to a low extinction. The near-field enhancement on the NP surface is thus low, and the near-field maxima occur in the dielectric layer between NPs [Figure 4a(vi)]. At 470 nm, the quadrupolar mode exhibits four lobes in the cross-section plane parallel to the incident polarization [Figures 4a(v) and S11e].

In comparison, the as-fabricated sample exhibits a much broader main dipolar peak than that of the regular sample, but its maximum also largely red-shifts from 500 to 634 nm when rotating the polarization from TM to TE [Figures S10b(iii) and 4b(iii)]. The second dipolar peak at the lower wavelength for TE polarization is less obvious, and it seems to interfere with the quadrupolar mode. The latter is less sensitive to the incident polarization, is broader than that for the regular sample, and occurs at 490 nm. The near-field intensity map on the cross section at 534 nm, where total extinction is the lowest, evidences a reduced field enhancement at the NP surface and a field maximum between NPs [Figure 4b(v)]. This behavior tends to evidence the destructive interference between the incidence and the waveguide mode although the corresponding effect is limited by the size heterogeneity and the spatial disorder of NPs. Indeed, as shown in the plane view of Figure 4b(v), some NP sizes resonate at 534 nm (red NPs). And, spatial disorder introduces phase variations between the field scattered by NPs along the *x* direction that reduce the coupling efficiency in the guided mode. Size heterogeneity and spatial disorder are thus limiting factors to observe the field enhancement at the long-wavelength peak in these laser-induced samples.

However, a strong dichroism is observed in these as-fabricated samples due to the difference between the main dipolar peaks obtained for TM and TE polarization. This dichroism is actually reinforced by another phenomenon that does not occur in the regular sample and that is highlighted in Figure 5: the near-field coupling between close NPs. The plane view of the near-field intensity at 634 nm in Figure 4b(vi) shows that different pairs of close NPs, found along the irregular lines, resonate at this wavelength (white rectangles). This near-field coupling leads to hybrid modes whose resonance frequencies are polarization-dependent and for which the high-frequency mode is usually a dark mode.[42−45] As shown in Figure 5, NP dimers embedded in a high index layer and tangent to the top interface, as described in Figure 3c, exhibit a dipolar resonance for TE polarization (the bright hybrid mode), the position of which red-shifts when the distance between NPs decreases. The narrow peak at around 470 nm that corresponds to a quadrupolar resonance also slightly red-shifts. As the gap decreases, the coupling between NPs increases and the near-field enhancement in the gap rises. Conversely, the resonance positions for TM polarization remain nearly unchanged, and the corresponding near-field map (Figure 5e,f) shows no indication of coupling between the resonance modes. These simulations demonstrate that the broad dipolar resonance of the as-fabricated samples that peaks at a low wavelength for TM [Figure S10b(iii)] and at a high

https://doi.org/10.1021/acsaom.3c00395
ACS Appl. Opt. Mater. 2024, 2, 373−385

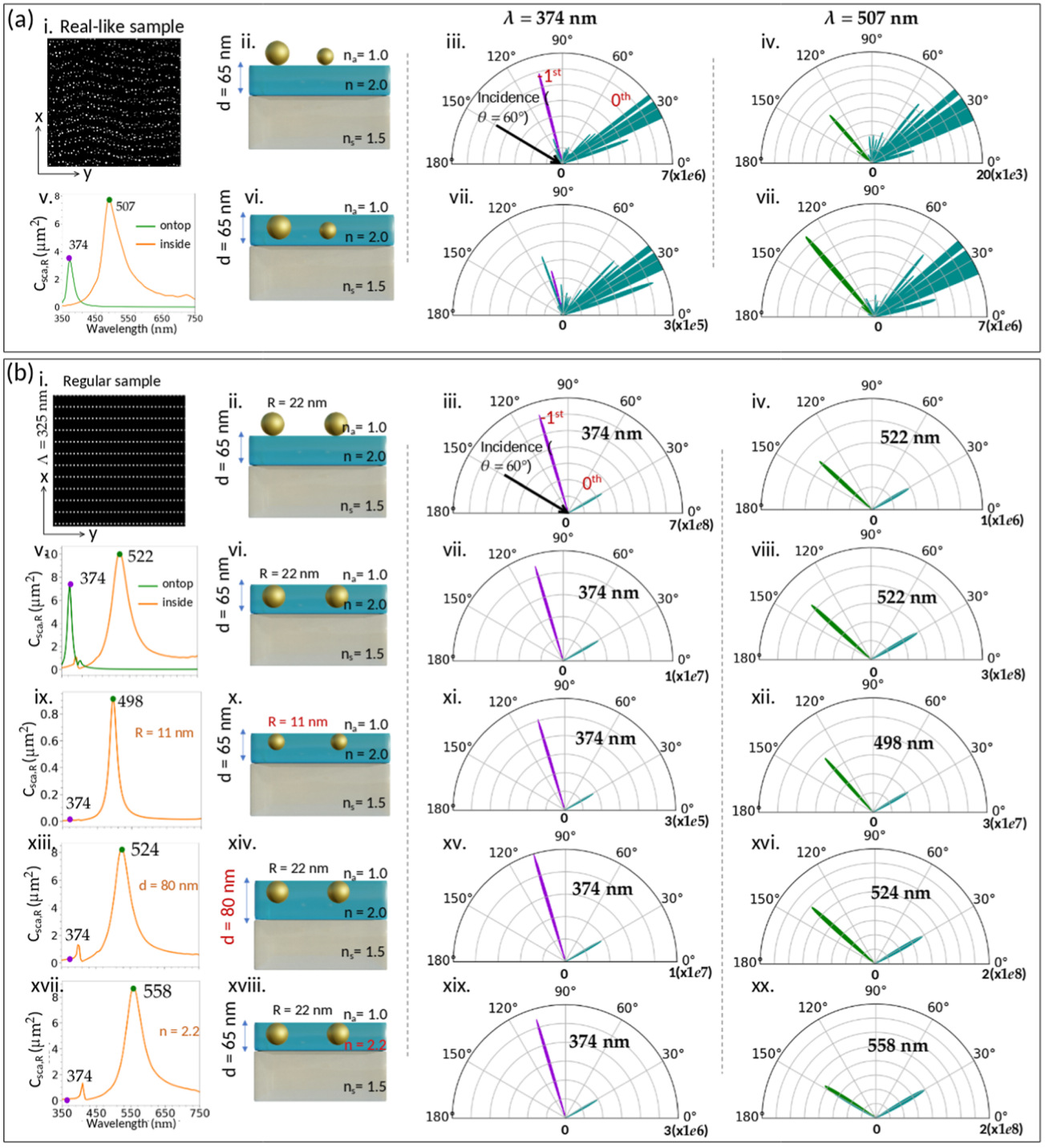

Figure 6. Influence of metasurface structural parameters on the diffraction. Plane view of the realistic (a(i)) and regular samples (b(i)). Scattering cross section in reflection side of realistic (a(v)) and regular (b(v,ix,xiii,xvii)) samples. Cross-section views of realistic (a(ii,vi)) and regular (b(ii,vi,x,xiv,xviii)) samples. Scattered radiation at the selected wavelengths of the realistic (a(iii,iv,vii,viii)) and regular (b-(iii,iv,vii,viii,xi,xii,xv,xvi,xix,xx)) samples. Unit of the differential scattering cross section is nm^2/steradian.

wavelength for TE [Figure 4b(iii)] is not only due to the size dispersion but also due to the variable distances between particles that lie along the same grating line. Many shoulder peaks appear in the TE polarization of the realistic sample [Figure 4b(iii)] attributed to the near-field coupling of NPs with different size and interparticle distance. Note that the small peaks at the shoulder of the broad dipolar resonances in TE polarization only appear when the NPs are embedded in a layer system, as shown in Figure S12. This small peak can be attributed to the interaction of the coupled dipolar resonance with the close air−TiO_2 interface. This small peak is not observed in the realistic sample because of the heterogeneous broadening of the dipolar resonance.

To summarize, the dichroic behavior of the extinction cross section of realistic samples results from two optical mechanisms. The first one originates from the near-field coupling between the LSPR of close NPs that can be found along the grating lines. It leads to mode hybridization with a

https://doi.org/10.1021/acsaom.3c00395
ACS Appl. Opt. Mater. 2024, 2, 373−385

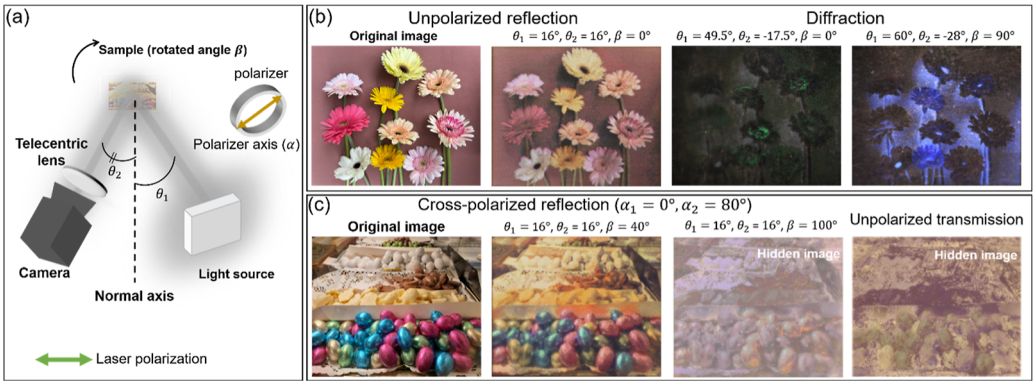

Figure 7. (a) Color acquisition setup for recording the printed images in different observation modes. The printed images are compared with the original ones. (b) Color printed image observed in unpolarized reflection and diffraction modes. (b) Color printed image observed in cross-polarized reflection (two polarizers are placed in front of the source and telecentric lens) and unpolarized transmission modes.

resonance position that is strongly dependent on the distance between close NPs and their respective diameter as well for TE polarization. The second one originates from the far-field coupling between the LSPR mode of NPs through the excitation of a photonic mode that interferes constructively with the incident field on the NPs at a specific wavelength that depends on the grating period. While carried out on specific samples, these results can be generalized to all metasurfaces, where self-organized NP gratings are observed.

Considerations on Diffraction by NP Gratings

Diffraction by the laser-induced metasurfaces shown in Figures 1 and 2 results either from surface topography gratings or from coherent scattering by self-organized NPs. While diffraction by periodic surface corrugation has been investigated in literature studies,[30,46] it is worth investigating the influence of some parameters of the NP arrays on diffraction. The study is based on the analysis of the spectral variations of the scattering cross section and the angular variations, in the incidence plane, of the differential scattering cross section (defined in Methods) at selected wavelengths. A sample is described in Figure S9 and is selected from Figure 1b based on its diffraction properties and the absence of surface modulation grating. This sample exhibits Ag NPs that are semiembedded at the top surface. An as-fabricated sample, modeled in Figure 6a, is created from the SEM plane view and TEM cross section and compared to the closest regular sample presented in Figure 6b in which 44 nm wide spherical NPs are separated by a period of 325 nm along the x direction and 100 nm along the y direction. As the semiembedded NPs cannot be simulated with the used modeling, two configurations are considered, with Ag NPs supported either on the TiO_2 surface or inside the TiO_2 layer where the biggest particles are tangent to the top interface (the relative positions of particles are kept unchanged in the two configurations).

The samples are illuminated by a TE-polarized plane wave under 60° of incidence (θ_i) from the top (air), with the incidence plane being perpendicular to the y-axis. The scattering cross sections in reflection of the realistic and regular samples exhibit similar spectra for both configurations, where Ag NPs are either in or out of the TiO_2 layer [Figure 6a(v),b(v)]. For particles inside the TiO_2 film, the main peak, corresponding to a dipolar mode, dominates the (orange) spectrum at 507 nm for the as-fabricated sample and 524 nm for the regular sample, while this dipolar peak blue-shifts in the violet region at 374 nm, respectively, when NPs are on top. Considering the period Λ = 325 nm for the as-fabricated and regular samples and using the grating equation $\sin(\theta_m) = \sin(\theta_i) - \lambda/\Lambda$, one can calculate the first diffraction angle at −43.9° for 507 nm, −48.3° for 524 nm, and −16.5° for 374 nm wavelength. These angles are actually the angles at which the maximum scattering efficiency is found on the left-end side of the angular scattering diagrams in Figure 6. It is interesting to note that the amplitude of the scattering cross-section maximum is almost the same for the as-fabricated and regular samples (slightly higher for the latter). However, the maximum diffracted intensity in the first diffraction order is 30−40 times higher in the regular sample than that in the as-fabricated sample if we compare the on-top configurations in the violet region and the inside configurations in the green region. This huge difference results from the heterogeneity of the as-fabricated sample that scatters a lot of light in a ±20° angular range around the specular direction, regardless of the wavelength. Note that as expected from the scattering spectra, the diffracted intensity in the violet first order is much higher for the on-top configurations than that for the inside configurations and vice versa in the green first diffraction order.

As observed from the characterizations of Figure S9, Ag NPs of the real sample are rather like Janus particles, with their top half located in the air and their bottom half located in the TiO_2. This sample is then expected to exhibit a maximum diffraction efficiency between violet and green. In fact, pictures (triangle #1) were taken with a diffraction angle of −28° to capture blue diffracted light, allowing for the visual observation of high diffraction intensity. One can also note that the exposure time of the camera was increased by 40 between the recording of diffraction images and the pictures recorded in the front side reflection mode. Our simulations thus fairly well match the experimental observations.

Simulations also allow for the study of the influence of some sample parameters individually. Figure 6b(ix)−(xii) shows that dividing the NP size by 2, from 44 to 22 nm, reduces the maximum diffraction intensity in the green first order by a factor 10. Increasing the TiO_2 thickness by 25% [Figure 6b(xiii)−(xvi)] or its refractive index by 10% [Figure 6b(xvii)−(xx)] slightly reduces the maximum diffraction efficiency in the green first order by a factor of 1.5.

To summarize the results about diffraction by NP gratings, one can keep in mind the following information. The grating period is fixed by the laser wavelength and the type of resonance excited during laser processing; the grating period

https://doi.org/10.1021/acsaom.3c00395
ACS Appl. Opt. Mater. 2024, 2, 373−385

determines the diffraction angle. The disorder that affects the spatial distribution of self-organized Ag NPs strongly reduces the diffraction efficiency, which, however, remains observable by the naked eye. The diffraction efficiency is significantly enhanced in the visible range when the Ag NPs are embedded in the top layer. Additionally, the higher the refractive index or thickness of the top layer, the lower the diffraction efficiency.

Printed Plasmonic Color Images

In this part, we show the degree of fidelity achievable through laser processing of quasi-random plasmonic metasurfaces in printing color images. We also demonstrate that targeted colors can be printed to be observed specifically in some modes of observation and disappear in other modes. This property is of interest for security printing. Contrary to ink-based techniques, which involve limited numbers of primary colors that are mixed together to create a full color image, laser processing prints as many primary colors as are present in the image to print. Each laser processing parameter set creates a specific type of metasurface that is associated with a given color in a particular mode of observation. The same laser-processed metasurface exhibits different colors in different modes of observation. Once the color databases observed in the different modes of observation are recorded by varying the laser processing parameters, one can implement a gamut mapping algorithm associated with a half-toning technique to print by laser color images that are as faithful as possible to the original image.[34] The resulting colors originate from the combination of scattering, absorption, diffraction, and interference. Figure 7 shows two images whose original colors were reproduced with a good fidelity either in a backside specular reflection observation mode (Figure 7b) or in a transmission observation mode involving polarized light (Figure 7c). The configurations of the observation modes are presented in Figure 7a. The image size is 13 × 11 mm^2 with a pixel size of 50 × 50 μm^2. Interestingly, the image in Figure 7b contains metasurfaces that diffract light in the plane of incidence either when the image is fixed horizontally on the measurement setup ($\beta = 0°$) or when it is rotated by $\beta = 90°$. Different images are then recorded with a diffraction measurement setup in which different parts are lit depending on the sample orientation. The combination of these images can be used to authenticate secured printing. Whitish areas that occur in the two diffraction images correspond to metasurfaces that scatter light over a broad range of wavelengths rather than diffracting it.

Figure 7c demonstrates the ability to reproduce faithfully different types of colors in a polarized observation mode, where the sample is placed between two polarizers whose axes form an angle of 80° and is observed in reflection. The selection of this specific angle is deliberate and aims to optimize the hue range in this polarized mode of observation. In this case, faithful colors are observed for a specific orientation of the sample between the two polarizers, and as soon as it is rotated in its plane (different β value) or observed under nonpolarized light, colors vanish. The sample observations under other modes are provided in Figure S13. These images indicate the wide variety of metasurfaces that can be produced by laser and combined to generate secured color images.

CONCLUSIONS

The article demonstrates the great potential of a single-step nanosecond laser-based technology for the production of metasurfaces with a wide range of optical properties. By variation of the processing parameters, metasurfaces that exhibit simultaneously or independently diffractive and dichroic properties can be produced. Using electromagnetic simulations, the article highlights the contribution of two optical mechanisms to the observed dichroism, which involve either the near-field coupling of close NPs located along the grating lines or the coherent far-field coupling between periodically spaced NP lines. The former results in the hybridization of LSPR modes and makes the resonance position strongly dependent on the distance between the close NPs for TE polarization only. The heterogeneity in size and distance of the hybridized pairs broadens the resonance but does not prevent the polarization sensitivity. The latter results in a near-field enhancement on the NP surface that is shifted toward the long wavelength for TE polarization only. The disorder and size dispersion attenuate the coupling strength. Furthermore, the observed diffraction originates from two main self-organization structures: NP gratings and surface topography gratings. The contribution of the NP gratings to diffraction is higher when they are embedded. Leveraging the optical properties of laser-induced metasurfaces, we successfully demonstrate the printing of color images, which can be observed in specific modes but are hidden in other modes. This technology exhibits great promise for advanced applications in the fields of security, display, or vision.

METHODS

Materials

The samples are made of mesoporous films of amorphous TiO_2 impregnated with silver salt and elaborated by a sol−gel process. The composition of the sol includes titanium tetraisopropoxide (TTIP, Aldrich; 97%), acetylacetone (AcAc, Aldrich; 99%), hydrochloric acid (HCl, Roth; 37%), ethanol (EtOH, Carlo Erba; absolute), Pluronic P123 ($(PEO)_{20}(PPO)_{70}(PEO)_{20}$, Aldrich; MW: 5000), and deionized water (H_2O) with the molar ratios: TTIP/P123/ethanol/HCl/H_2O/AcAc = 1:0.025:28.5:0.015:29.97:0.5. The mesoporous titania films, with a thickness of 200 ± 30 nm, are formed by dip-coating and calcination at 340 °C. The films are then soaked in a silver nitrate solution (0.85 M) for 30 min. After rinsing and drying, the final step is UV exposure (5 min) at 400 $\mu W \cdot cm^{-2}$ and 254 nm.

Laser Processing

A nanosecond fiber laser, with a pulse duration of 1.3 at 532 nm from IPG photonics, is used to scan on the material surface equipped with a galvanometric mirror scanner head (Sunny Technology). The laser is the focus on the sample by using a 16 cm F-Theta lens with a focused laser spot size of 13.5 μm at 1/e and is linearly polarized using a Brewster angle polarizer, where the polarization can be controlled by using a half-wave plate (as sketched in Figure S1). The laser fluences can be calculated from the relation

$$F = \frac{2P}{f_{rep} \cdot \pi r^2} \ (J/cm^2)$$

where P is the laser power, f_{rep} (Hz) is the repetition rate, and r is the beam radius at 1/e. The metasurfaces shown in Figure 1 are produced with a 50 × 50 μm^2 pixel size by drawing consecutive laser lines parallel to the horizontal axis, whose distances between the lines are dy = 2 and 20 μm. The pictures in Figure 7 are drawn with a 50 × 50 μm^2 pixel size over an area of 13 × 11 mm^2 and by the diagonal laser lines with the interline distance dy = 10 μm (detailed in Figure S2, Supporting Information).

Electromagnetic Simulation

The simulations are carried out using the T-matrix-based method,[47] written in Python as SMUTHI.[48] The method allows the optical

https://doi.org/10.1021/acsaom.3c00395
ACS Appl. Opt. Mater. 2024, 2, 373−385

responses to be calculated in near field or far field of an NP ensemble near or on dielectric surfaces. The extinction cross section usually refers to the summation of the scattering cross section and absorption cross section when particles are surrounded by a homogeneous medium. However, when particles are close to planar surfaces, it is more convenient to divide the extinction cross section into transmission side ($C_{ext,T}$) and reflection side ($C_{ext,R}$) and derived from the ratio of the time-averaged power lost in the transmitted direction $\langle P_{ext,T}\rangle$ or reflected direction $\langle P_{ext,R}\rangle$ to the incident intensity (I_0) as $C_{ext,T} = -\langle P_{ext,T}\rangle/I_0$, $C_{ext,R} = -\langle P_{ext,R}\rangle/I_0$.[49] The differential scattering cross section, on the other hand, is defined as $\sigma_{\Omega,sca} = I^{-1}\, d\langle\phi_{sca}\rangle/d\Omega$, where I is the intensity of the plane wave in top or bottom interface area, $\langle\phi_{sca}\rangle$ is the time-averaged radiant flux of the scattered field, and Ω is the solid angle. The scattering cross section is then the integral of the different cross sections over the solid angle $\sigma_{sca} = \int d^2\,\Omega\sigma_{\Omega,sca}$.

Notice that, for all the simulations, the NP arrays are reproduced from the NP distribution of the real sample, and then, the obtained area is duplicated four times. The duplicated samples are constructed from the obtained area, where the width and height are w_y and h_x and the coordinate in the xy plane is x_0 and y_0, and its three copies with the same size and the coordinates are $x_1 = x_0 + h_x + a$, $y_1 = y_0$; $x_2 = x_0$, $y_2 = y_0 + w_y + b$; $x_3 = x_0 + h_x + a$, $y_3 = y_0 + w_y + b$, with a = 300 (nm) and b = 100 (nm) for the simulations in Figures 3 and 4 and a = 325 (nm) and b = 100 (nm) for the simulations in Figure 6.

Silver permittivity obtained from the modified Drude model

$$\epsilon(\omega) = \epsilon_{ib} - \frac{\omega_p^2 \epsilon_0}{\omega^2 + j\omega\Gamma}$$

where $\epsilon_{ib} = 3.7\epsilon_0$ is the contribution of interband transition, ϵ_0 is the vacuum permittivity, ω_p is the frequency of plasma resonance with $\hbar\omega_p$ = 8.89 eV, and $\Gamma = \Gamma_0 + Av_F/r$ is the damping constant with Γ_0 = 17.6 meV the damping constant of bulk silver, A = 1 a constant, $v_f = 1.39 \times 10^6$ m/s the Fermi velocity, and r the particle radius.

Morphological Characterizations

A FEI Nova NanoSEM 200 scanning electron microscope in a low-vacuum mode and a helix detector are used to measure the plane views of the samples. The cross-section view and chemical analysis are performed using a Jeol 2021 TEM instrument operated at 200 kV. FIB lamellae are produced with a FIB-FEI Helios 600i instrument.

Sample surface profiles are measured using a Bruker Icon atomic force microscope (AFM.

■ ASSOCIATED CONTENT

Supporting Information

The Supporting Information is available free of charge at https://pubs.acs.org/doi/10.1021/acsaom.3c00395.

> Additional experimental details (laser setup, description of laser drawing lines, and color characterization), description of the origin of self-organized periodic patterns, additional sample characterizations (SEM, AFM, TEM, and Raman analysis), near-field map for TM polarization, and printed images observed in other modes (PDF)

■ AUTHOR INFORMATION

Corresponding Author

Nathalie Destouches − *Univ Lyon, UJM-Saint-Etienne, CNRS, Institut d'Optique Graduate School, Laboratoire Hubert Curien UMR 5516, Saint-Etienne F-42023, France;* orcid.org/0000-0002-3843-6382;
Email: nathalie.destouches@univ-st-etienne.fr

Authors

Van Doan Le − *Univ Lyon, UJM-Saint-Etienne, CNRS, Institut d'Optique Graduate School, Laboratoire Hubert Curien UMR 5516, Saint-Etienne F-42023, France;* orcid.org/0000-0003-2020-170X

Balint Eles − *Univ Lyon, UJM-Saint-Etienne, CNRS, Institut d'Optique Graduate School, Laboratoire Hubert Curien UMR 5516, Saint-Etienne F-42023, France;* orcid.org/0000-0003-1279-3434

Nicolas Dalloz − *Univ Lyon, UJM-Saint-Etienne, CNRS, Institut d'Optique Graduate School, Laboratoire Hubert Curien UMR 5516, Saint-Etienne F-42023, France; HID Global CID SAS, Suresnes 92100, France*

Manuel A. Flores Figueroa − *Univ Lyon, UJM-Saint-Etienne, CNRS, Institut d'Optique Graduate School, Laboratoire Hubert Curien UMR 5516, Saint-Etienne F-42023, France*

Francis Vocanson − *Univ Lyon, UJM-Saint-Etienne, CNRS, Institut d'Optique Graduate School, Laboratoire Hubert Curien UMR 5516, Saint-Etienne F-42023, France*

Christophe Hubert − *Univ Lyon, UJM-Saint-Etienne, CNRS, Institut d'Optique Graduate School, Laboratoire Hubert Curien UMR 5516, Saint-Etienne F-42023, France*

Complete contact information is available at: https://pubs.acs.org/10.1021/acsaom.3c00395

Notes

The authors declare no competing financial interest.

■ ACKNOWLEDGMENTS

This work is funded by the ANR project MIXUP (ANR-18-CE39-0010). The authors thank David Troadec from the IEMN laboratory for the FIB lamella preparation. V.D.L. thanks Amos Egel (Hembach Photonik GmbH) for fruitful discussions on using SMUTHI.

■ REFERENCES

(1) Kristensen, A.; Yang, J. K. W.; Bozhevolnyi, S. I.; Link, S.; Nordlander, P.; Halas, N. J.; Mortensen, N. A. Plasmonic Colour Generation. *Nat. Rev. Mater.* **2017**, *2*, 16088.

(2) Dumanli, A. G.; Savin, T. Recent Advances in the Biomimicry of Structural Colours. *Chem. Soc. Rev.* **2016**, *45*, 6698−6724.

(3) Neubrech, F.; Duan, X.; Liu, N. Dynamic Plasmonic Color Generation Enabled by Functional Materials. *Sci. Adv.* **2020**, *6*, No. eabc2709.

(4) Vynck, K.; Pacanowski, R.; Agreda, A.; Dufay, A.; Granier, X.; Lalanne, P. The Visual Appearances of Disordered Optical Metasurfaces. *Nat. Mater.* **2022**, *21*, 1035−1041.

(5) Hsu, C. W.; Zhen, B.; Qiu, W.; Shapira, O.; DeLacy, B. G.; Joannopoulos, J. D.; Soljačić, M. Transparent Displays Enabled by Resonant Nanoparticle Scattering. *Nat. Commun.* **2014**, *5*, 3152.

(6) Cheng, F.; Gao, J.; Luk, T. S.; Yang, X. Structural Color Printing Based on Plasmonic Metasurfaces of Perfect Light Absorption. *Sci. Rep.* **2015**, *5*, 11045.

(7) Song, M.; Kudyshev, Z. A.; Yu, H.; Boltasseva, A.; Shalaev, V. M.; Kildishev, A. V. Achieving Full-Color Generation with Polarization-Tunable Perfect Light Absorption. *Opt. Mater. Express* **2019**, *9*, 779.

(8) Duempelmann, L.; Casari, D.; Luu-Dinh, A.; Gallinet, B.; Novotny, L. Color Rendering Plasmonic Aluminum Substrates with Angular Symmetry Breaking. *ACS Nano* **2015**, *9*, 12383−12391.

(9) Jiang, H.; Kaminska, B. Scalable Inkjet-Based Structural Color Printing by Molding Transparent Gratings on Multilayer Nanostructured Surfaces. *ACS Nano* **2018**, *12*, 3112−3125.

(10) Clausen, J. S.; Højlund-Nielsen, E.; Christiansen, A. B.; Yazdi, S.; Grajower, M.; Taha, H.; Levy, U.; Kristensen, A.; Mortensen, N. A. Plasmonic Metasurfaces for Coloration of Plastic Consumer Products. *Nano Lett.* **2014**, *14*, 4499−4504.
(11) Caligiuri, V.; Patra, A.; De Santo, M. P.; Forestiero, A.; Papuzzo, G.; Aceti, D. M.; Lio, G. E.; Barberi, R.; De Luca, A. Hybrid Plasmonic/Photonic Nanoscale Strategy for Multilevel Anticounterfeit Labels. *ACS Appl. Mater. Interfaces* **2021**, *13*, 49172−49183.
(12) Gu, Y.; Zhang, L.; Yang, J. K. W.; Yeo, S. P.; Qiu, C.-W. Color Generation *via* Subwavelength Plasmonic Nanostructures. *Nanoscale* **2015**, *7*, 6409−6419.
(13) Liu, H.; Xu, J.; Wang, H.; Liu, Y.; Ruan, Q.; Wu, Y.; Liu, X.; Yang, J. K. W. Tunable Resonator-Upconverted Emission (TRUE) Color Printing and Applications in Optical Security. *Adv. Mater.* **2019**, *31*, 1807900.
(14) Hong, W.; Yuan, Z.; Chen, X. Structural Color Materials for Optical Anticounterfeiting. *Small* **2020**, *16*, 1907626.
(15) Duempelmann, L.; Luu-Dinh, A.; Gallinet, B.; Novotny, L. Four-Fold Color Filter Based on Plasmonic Phase Retarder. *ACS Photonics* **2016**, *3*, 190−196.
(16) Mohammadi, R.; Ochs, M.; Andrieu-Brunsen, A.; Vogel, N. Effect of Asymmetry on Plasmon Hybridization and Sensing Capacities of Hole-Disk Arrays. *J. Phys. Chem. C* **2020**, *124*, 2609−2618.
(17) Xiong, K.; Tordera, D.; Jonsson, M. P.; Dahlin, A. B. Active Control of Plasmonic Colors: Emerging Display Technologies. *Rep. Prog. Phys.* **2019**, *82*, 024501.
(18) Roberts, A. S.; Pors, A.; Albrektsen, O.; Bozhevolnyi, S. I. Subwavelength Plasmonic Color Printing Protected for Ambient Use. *Nano Lett.* **2014**, *14*, 783−787.
(19) Ng, R. J. H.; Krishnan, R. V.; Wang, H.; Yang, J. K. W. Darkfield Colors from Multi-Periodic Arrays of Gap Plasmon Resonators. *Nanophotonics* **2020**, *9*, 533−545.
(20) Manzano, C. V.; Ramos, D.; Pethö, L.; Bürki, G.; Michler, J.; Philippe, L. Controlling the Color and Effective Refractive Index of Metal-Anodic Aluminum Oxide (AAO)-Al Nanostructures: Morphology of AAO. *J. Phys. Chem. C* **2018**, *122*, 957−963.
(21) Zhu, X.; Vannahme, C.; Højlund-Nielsen, E.; Mortensen, N. A.; Kristensen, A. Plasmonic Colour Laser Printing. *Nat. Nanotechnol.* **2016**, *11*, 325−329.
(22) Zhu, X.; Engelberg, J.; Remennik, S.; Zhou, B.; Pedersen, J. N.; Uhd Jepsen, P.; Levy, U.; Kristensen, A. Resonant Laser Printing of Optical Metasurfaces. *Nano Lett.* **2022**, *22*, 2786−2792.
(23) Zhang, Y.; Zhang, Q.; Ouyang, X.; Lei, D. Y.; Zhang, A. P.; Tam, H.-Y. Ultrafast Light-Controlled Growth of Silver Nanoparticles for Direct Plasmonic Color Printing. *ACS Nano* **2018**, *12*, 9913−9921.
(24) Zhang, Y.; Liang, Z.; Zhang, A. P.; Tam, H. Direct Printing of Micropatterned Plasmonic Substrates of Size-Controlled Gold Nanoparticles by Precision Photoreduction. *Adv. Optical Mater.* **2021**, *9*, 2001368.
(25) Chowdhury, S. N.; Nyga, P.; Kudyshev, Z. A.; Garcia Bravo, E.; Lagutchev, A. S.; Kildishev, A. V.; Shalaev, V. M.; Boltasseva, A. Lithography-Free Plasmonic Color Printing with Femtosecond Laser on Semicontinuous Silver Films. *ACS Photonics* **2021**, *8*, 521−530.
(26) Hwang, J. S.; Arthanari, S.; Ko, P.; Jung, K.; Park, J.-E.; Youn, H.; Yang, M.; Kim, S.-W.; Lee, H.; Kim, Y.-J. Plasmonic Color Printing via Bottom-Up Laser-Induced Photomodification Process. *ACS Appl. Mater. Interfaces* **2022**, *14*, 30315−30323.
(27) Wang, Y.; Ren, F.; Ding, T. Generation of High Quality, Uniform and Stable Plasmonic Colorants via Laser Direct Writing. *Adv. Optical Mater.* **2020**, *8*, 2000164.
(28) Roberts, A. S.; Novikov, S. M.; Yang, Y.; Chen, Y.; Boroviks, S.; Beermann, J.; Mortensen, N. A.; Bozhevolnyi, S. I. Laser Writing of Bright Colors on Near-Percolation Plasmonic Reflector Arrays. *ACS Nano* **2019**, *13*, 71−77.
(29) Sharma, N.; Vangheluwe, M.; Vocanson, F.; Cazier, A.; Bugnet, M.; Reynaud, S.; Vermeulin, A.; Destouches, N. Laser-Driven Plasmonic Gratings for Hiding Multiple Images. *Mater. Horiz.* **2019**, *6*, 978−983.
(30) Florian, C.; Kirner, S. V.; Krüger, J.; Bonse, J. Surface Functionalization by Laser-Induced Periodic Surface Structures. *J. Laser Appl.* **2020**, *32*, 022063.
(31) Liu, Z.; Siegel, J.; Garcia-Lechuga, M.; Epicier, T.; Lefkir, Y.; Reynaud, S.; Bugnet, M.; Vocanson, F.; Solis, J.; Vitrant, G.; Destouches, N. Three-Dimensional Self-Organization in Nanocomposite Layered Systems by Ultrafast Laser Pulses. *ACS Nano* **2017**, *11*, 5031−5040.
(32) Sharma, N.; Destouches, N.; Florian, C.; Serna, R.; Siegel, J. Tailoring Metal-Dielectric Nanocomposite Materials with Ultrashort Laser Pulses for Dichroic Color Control. *Nanoscale* **2019**, *11*, 18779−18789.
(33) Destouches, N.; Sharma, N.; Vangheluwe, M.; Dalloz, N.; Vocanson, F.; Bugnet, M.; Hébert, M.; Siegel, J. Laser-Empowered Random Metasurfaces for White Light Printed Image Multiplexing. *Adv. Funct. Mater.* **2021**, *31*, 2010430.
(34) Dalloz, N.; Le, V. D.; Hebert, M.; Eles, B.; Flores Figueroa, M. A.; Hubert, C.; Ma, H.; Sharma, N.; Vocanson, F.; Ayala, S.; Destouches, N. Anti-Counterfeiting White Light Printed Image Multiplexing by Fast Nanosecond Laser Processing. *Adv. Mater.* **2022**, *34*, 2104054.
(35) Veiko, V. P.; Andreeva, Y.; Van Cuong, L.; Lutoshina, D.; Polyakov, D.; Sinev, D.; Mikhailovskii, V.; Kolobov, Y. R.; Odintsova, G. Laser Paintbrush as a Tool for Modern Art. *Optica* **2021**, *8*, 577.
(36) Andreeva, Ya. M.; Luong, V. C.; Lutoshina, D. S.; Medvedev, O. S.; Mikhailovskii, V. Yu.; Moskvin, M. K.; Odintsova, G. V.; Romanov, V. V.; Shchedrina, N. N.; Veiko, V. P. Laser Coloration of Metals in Visual Art and Design. *Opt. Mater. Express* **2019**, *9*, 1310.
(37) Liu, Z.; Destouches, N.; Vitrant, G.; Lefkir, Y.; Epicier, T.; Vocanson, F.; Bakhti, S.; Fang, Y.; Bandyopadhyay, B.; Ahmed, M. Understanding the Growth Mechanisms of Ag Nanoparticles Controlled by Plasmon-Induced Charge Transfers in Ag-TiO_2 Films. *J. Phys. Chem. C* **2015**, *119*, 9496−9505.
(38) Ma, H.; Bakhti, S.; Rudenko, A.; Vocanson, F.; Slaughter, D. S.; Destouches, N.; Itina, T. E. Laser-Generated Ag Nanoparticles in Mesoporous TiO_2 Films: Formation Processes and Modeling-Based Size Prediction. *J. Phys. Chem. C* **2019**, *123*, 25898−25907.
(39) Le, V. D.; Lefkir, Y.; Destouches, N. Hybridization between plasmonic and photonic modes in laser-induced self-organized quasi-random plasmonic metasurfaces. *Nanoscale* **2023**, *15*, 19339−19350.
(40) Sarkar, S.; Gupta, V.; Kumar, M.; Schubert, J.; Probst, P. T.; Joseph, J.; König, T. A. Hybridized Guided-Mode Resonances via Colloidal Plasmonic Self-Assembled Grating. *ACS Appl. Mater. Interfaces* **2019**, *11*, 13752−13760.
(41) Linden, S.; Kuhl, J.; Giessen, H. Controlling the Interaction between Light and Gold Nanoparticles: Selective Suppression of Extinction. *Phys. Rev. Lett.* **2001**, *86*, 4688−4691.
(42) Tsai, C.-Y.; Lin, J.-W.; Wu, C.-Y.; Lin, P.-T.; Lu, T.-W.; Lee, P.-T. Plasmonic Coupling in Gold Nanoring Dimers: Observation of Coupled Bonding Mode. *Nano Lett.* **2012**, *12*, 1648−1654.
(43) Yang, S.-C.; Kobori, H.; He, C.-L.; Lin, M.-H.; Chen, H.-Y.; Li, C.; Kanehara, M.; Teranishi, T.; Gwo, S. Plasmon Hybridization in Individual Gold Nanocrystal Dimers: Direct Observation of Bright and Dark Modes. *Nano Lett.* **2010**, *10*, 632−637.
(44) Jain, P. K.; Huang, W.; El-Sayed, M. A. On the Universal Scaling Behavior of the Distance Decay of Plasmon Coupling in Metal Nanoparticle Pairs: A Plasmon Ruler Equation. *Nano Lett.* **2007**, *7*, 2080−2088.
(45) Bakhti, S.; Destouches, N.; Tishchenko, A. V. Coupled Mode Modeling To Interpret Hybrid Modes and Fano Resonances in Plasmonic Systems. *ACS Photonics* **2015**, *2*, 246−255.
(46) Bonse, J.; Hohm, S.; Kirner, S. V.; Rosenfeld, A.; Kruger, J. Laser-Induced Periodic Surface Structures— A Scientific Evergreen. *IEEE J. Select. Topics Quantum Electron.* **2017**, *23*, 7581030.
(47) Egel, A.; Lemmer, U. Dipole Emission in Stratified Media with Multiple Spherical Scatterers: Enhanced Outcoupling from OLEDs. *J. Quant. Spectrosc. Radiat. Transfer* **2014**, *148*, 165−176.

https://doi.org/10.1021/acsaom.3c00395
ACS Appl. Opt. Mater. 2024, 2, 373−385

(48) Egel, A.; Czajkowski, K. M.; Theobald, D.; Ladutenko, K.; Kuznetsov, A. S.; Pattelli, L. SMUTHI: A Python Package for the Simulation of Light Scattering by Multiple Particles near or between Planar Interfaces. *J. Quant. Spectrosc. Radiat. Transfer* **2021**, *273*, 107846.
(49) Egel, A. Accurate Optical Simulation of Disordered Scattering Layers for Light Extraction from Organic Light Emitting Diodes. Doctoral Dissertation, Karlsruhe Institute of Technology (KIT), 2018.

https://doi.org/10.1021/acsaom.3c00395
ACS Appl. Opt. Mater. 2024, 2, 373−385